


## Article

# Impacts of Space Restriction on the Microstructure of Calcium Silicate Hydrate

Yue Zhou <sup>1,2</sup> , Zhongping Wang <sup>1,2</sup>, Zheyu Zhu <sup>1,2</sup>, Yuting Chen <sup>1,2</sup>, Linglin Xu <sup>1,2,\*</sup> and Kai Wu <sup>1,2</sup>

<sup>1</sup> School of Materials Science and Engineering, Tongji University, 4800 Cao'an Road, Shanghai 201804, China; 1710816@tongji.edu.cn (Y.Z.); wangzpk@tongji.edu.cn (Z.W.); 17712937215@163.com (Z.Z.); 1930649@tongji.edu.cn (Y.C.); wukai@tongji.edu.cn (K.W.)

<sup>2</sup> Key Laboratory of Advanced Civil Engineering Materials, Tongji University, Ministry of Education, 4800 Cao'an Road, Shanghai 201804, China

\* Correspondence: xulinglinok@hotmail.com; Tel.: +86-21-6958-2144

**Abstract:** The effect of hydration space on cement hydration is essential. After a few days, space restriction affects the hydration kinetics which dominate the expansion, shrinkage and creep of cement materials. The influence of space restriction on the hydration products of tricalcium silicate was studied in this paper. The microstructure, morphology and composition of calcium silicate hydrate (C-S-H) were explored from the perspective of a specific single micropore. A combination of Raman spectra, Fourier transform infrared spectra, scanning electron microscopy and energy dispersive X-ray spectroscopy were employed. The results show that space restriction affects the structure of the hydration products. The C-S-H formed in the micropores was mainly composed of Q<sup>3</sup> silicate tetrahedra with a high degree of polymerization. The C-S-H formed under standard conditions with a water to cement ratio of 0.5 mostly existed as Q<sup>2</sup> units. Space restriction during hydration is conducive to the formation of C-S-H with silica tetrahedra of a high polymerization degree, while the amount of water filling the micropore plays no obvious role on the polymeric structure of C-S-H during hydration.

**Keywords:** calcium silicate hydrate (C-S-H); space restriction; cement; hydration



**Citation:** Zhou, Y.; Wang, Z.; Zhu, Z.; Chen, Y.; Xu, L.; Wu, K. Impacts of Space Restriction on the Microstructure of Calcium Silicate Hydrate. *Materials* **2021**, *14*, 3645. <https://doi.org/10.3390/ma14133645>

Academic Editor: Neven Ukrainczyk

Received: 24 May 2021  
Accepted: 27 June 2021  
Published: 30 June 2021

**Publisher's Note:** MDPI stays neutral with regard to jurisdictional claims in published maps and institutional affiliations.



**Copyright:** © 2021 by the authors. Licensee MDPI, Basel, Switzerland. This article is an open access article distributed under the terms and conditions of the Creative Commons Attribution (CC BY) license (<https://creativecommons.org/licenses/by/4.0/>).

## 1. Introduction

As the dominating hydration product of Portland cement, calcium silicate hydrate (C-S-H) plays a key role in the performance of cementitious materials. C-S-H grows when the cement is mixed with water [1], and this hydration continues until the water is exhausted [2]. Its structure varies with factors during hydration, especially the water to binder ratio [3,4], temperature [5–8] and curing age [6,9]. The growth of C-S-H involves the competition between water and hydration space, which are also essential to the microstructure evolution. The importance of water to the structure of C-S-H is prominent, and the role of space on the structure of C-S-H has been paid more and more attention, especially for those studies on the kinetics and mechanisms of cement hydration.

As the main constituent of Portland cement, the hydration of alite (C<sub>3</sub>S) is essential and it can be divided into three periods [2,10]. Initially, C<sub>3</sub>S massively dissolves and amorphous nanoglobular C-S-H mainly forms in this period (Period I) [11]. There is sufficient space at this stage. Then the hydration switches to the main hydration period (Period II). The C-S-H explosively grows and the hydration rate experiences a stage of acceleration to deceleration [2]. The initial space is continuously filled with hydration products. Initially, C-S-H grows rapidly to a certain length on the cement grains as needle morphology [12]. When it has covered most of the grain surface, this stage is related to the deceleration stage [12]. Then the hydration comes to period III, the later stages [13]. The C-S-H around the grain surface forms a shell which controls the inner space and available water outside. The growth of inner C-S-H is accompanied by a lack of space and water. Meanwhile, the

outer C-S-H further fill the space at this stage [14]. The space filling hypothesis is suggested to dominate the later hydration mechanism [2]. The C-S-H which forms in the later stage grows in a diminishing, restricted space. In general, those unhydrated phases undergo a state transition from sufficiency to a restriction of space.

The growth of C-S-H and available space are inseparable. Recent research has proposed that the initial space occupied by water is the space where the C-S-H can grow [2]. The  $^1\text{H}$  nuclear magnetic resonance is used to divide the “water space” in the cement paste into three types: interlayer water between C-S-H layers, gel pores and capillary pores [15,16]. The growth of hydrates in the capillary space is related to the expansion of the hardened cement matrix, due to crystallization pressure [10,17]. The crystals grown in the pores and also the pore walls generate stress to prevent crystal growth. Eventually, the crystals exert pressure on the surrounding solid phase [17]. The pore space affects the shrinkage and creep of the cement paste at the late hydration stage [18,19]. Thus space is considered a key factor for the construction of the C-S-H microstructure model. The classical C-S-H model proposed by Jennings describes two types of C-S-H: low-density C-S-H (LD C-S-H) and high-density C-S-H (HD C-S-H) [20,21]. LD C-S-H forms in the early hydration stage when there is enough capillary space to accommodate C-S-H [22]. With the proceeding of hydration, the continuous filling by hydration products leads to more restriction in the space, which drives LD C-S-H to HD C-S-H [22,23]. This finding indicates that the space limitation is firmly related to the diversity of C-S-H. Nanoindentation results show that HD C-S-H exhibits higher stiffness [24]. The difference in performance actually reflects the change in the microstructure of C-S-H.

The microstructure of C-S-H is commonly expressed by the polymerization degree of silicate tetrahedra. The  $Q^n$  classification is used to represent the Si-environments in silicate tetrahedra with different polymerization degrees, where  $n$  stands for the number of oxygen atoms shared between the tetrahedra and its adjacent tetrahedra [25,26]. Studies show that the silicate tetrahedra of C-S-H in cement are mainly dimers ( $Q^1$  Si sites), with few trimer ( $Q^2$  Si sites) [27–29]. The silicate tetrahedra in tobermorite and jennite, which are used as reference when constructing the C-S-H model, with repeating structure of “dreierkette” and the ratio of  $Q^2$  and  $Q^3$  units are much higher than those of  $Q^1$  units [27,28]. Studies indicate that the polymerization degree of C-S-H increases with curing age [6,30,31], while the available space decreases over time, simultaneously. There are many mysteries between the formation of highly polymerized units and space restriction.

During the entire hydration, the “water space” is gradually filled by the growing hydrates and undergoes a process from micrometer to nanometer scale. Therefore, the influence of the space restriction on the structure of C-S-H is explored from the perspective of a single micropore in this paper.

## 2. Materials and Methods

### 2.1. Sample Preparation

The pure M3 tricalcium silicate ( $\text{C}_3\text{S}$ ) was prepared by calcination. Magnesium was used to stabilize  $\text{C}_3\text{S}$  with polymorph M3. The amount of chemically pure calcium oxide (CaO) and silicon dioxide ( $\text{SiO}_2$ ) with a molar ratio of 3.0 was accurately weighed, and MgO was added in an amount of 2% of the total mass. The raw materials were uniformly mixed and put into a platinum crucible. Then the crucible was put into the furnace and calcinated at  $1400\text{ }^\circ\text{C}$  for 4 h. After that, the sample was cooled to room temperature and ground into powder. To obtain the pure M3 polymorph  $\text{C}_3\text{S}$ , this treatment was repeated 3 times. The phase composition was analyzed by XRD (Rigaku International Corporation, Akishima, Tokyo, Japan) and the pattern is shown in Figure 1.

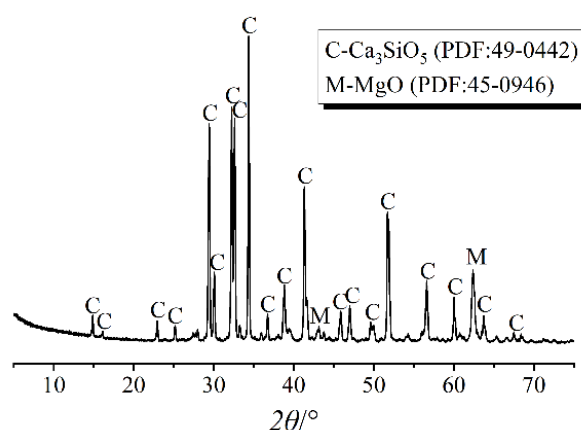


**Figure 1.** XRD patterns of  $C_3S$ .

The experiment was based on a stainless steel sheet customized by Shanghai Guangyan Laser Technology Co. (Room 896, No.235 Changyang Road, Hongkou District, Shanghai, China), Ltd. (the size was  $5\text{ mm} \times 5\text{ mm}$ , and the thickness was  $100\ \mu\text{m}$ ). A  $4 \times 5$  pore array was made on the sheet by a 50 w optical fiber marking machine, as shown in Figure 2. The diameter of the pores was  $10 \pm 5\ \mu\text{m}$ , and these pores did not penetrate the sheet.

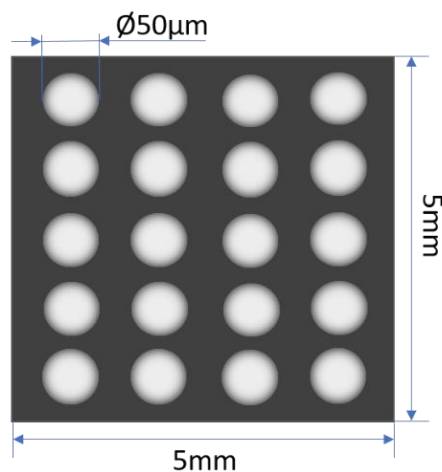


**Figure 2.** Schematic diagram of stainless steel sheet with pore array.

$C_3S$  particles were placed in micropores (Shanghai Guangyan Laser Technology Co, Shanghai, China) of the sheet with a tweezer under a microscope. These samples were treated by two methods. On the one hand, the sheet was covered by a drop of deionized water and was placed at  $20\ ^\circ\text{C}$  and 65% relative humidity (RH) for 24 h (hereafter called water condition). On the other hand, the sheet was placed in the curing room at  $20\ ^\circ\text{C}$  and 65% RH for 24 h without further addition of water (hereafter called 65% RH condition). Meanwhile,  $C_3S$  was mixed with deionized water at a water to cement ratio of 0.5 and hydrated for 24 h under the same curing conditions, as the control. The hydration was terminated via the freeze-vacuum drying for 48 h.

## 2.2. Analytical Methods

Raman spectra were collected by the LabRAM HR Evolution Raman Spectrometer (HORIBA Jobin Yvon, Paris, France) from HORIBA Jobin Yvon, France. A solid-state laser with a wavelength of 532 nm was used as the light source and the acquisition time was 10 s. The spectra were obtained with a  $100\times$  magnification. A micro area in a single pore of the sheet was selected for testing. Five pores were randomly selected for testing.

Fourier transform infrared spectra (FT-IR) were recorded using the EQUINOX 55 Fourier transform infrared spectrometer (Bruker, Karlsruhe, Baden-Württemberg, Ger-

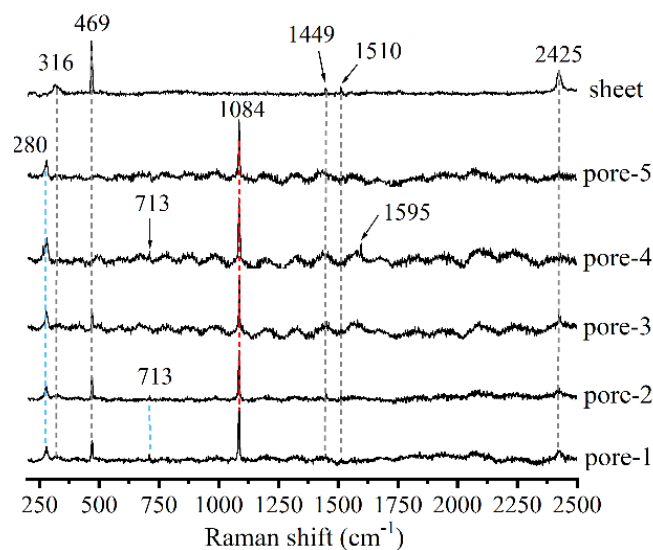
many) from Bruker and the MIRacle ATR measurement accessory (PIKE Technologies, Madison, WI, USA) from PIKE Technologies, USA. The ATR sample cell was made of ZnSe crystal. The sheet was placed in the sample cell and all pores were tested simultaneously. Each spectrum was acquired with 128 scans and at a resolution of  $4\text{ cm}^{-1}$ .

The morphology of samples was obtained by the Gemini Sigma 300/VP scanning electron microscope (SEM) (Carl Zeiss, Oberkochen, Baden-Württemberg, Germany) from Carl Zeiss, Germany. The images were acquired employing an acceleration voltage of 30 kV under high vacuum conditions. The elemental analysis was collected by the X-Max<sup>N</sup> spectrometer (Oxford Instruments, Abingdon, Oxfordshire, UK) of Oxford Instruments (EDS) and combined with Aztec software (Version 3.2, Oxford Instruments, Abingdon, Oxfordshire, UK).

### 3. Results

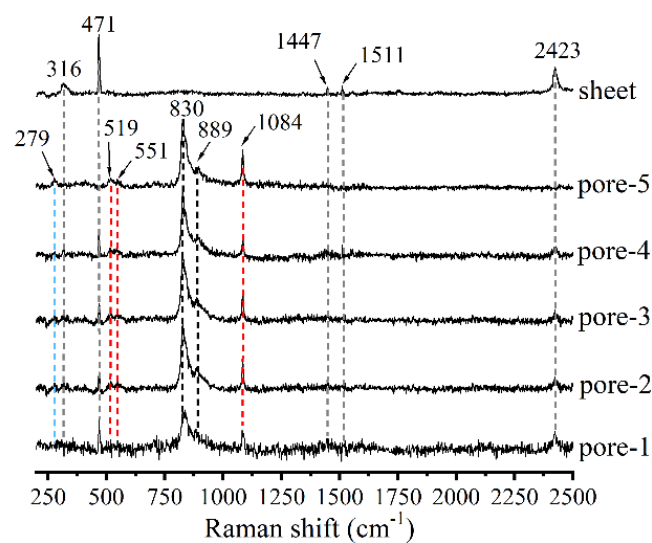
#### 3.1. Raman

Figure 3 shows the Raman spectra of the hydration products in different pores which were treated by the water conditions. Besides those shifts at 316, 469, 1449, 1510 and  $2425\text{ cm}^{-1}$  from the sheet, there was a strong and sharp peak at  $1084\text{ cm}^{-1}$  in all pores. This peak may be assigned to the symmetrical stretching of  $Q^3$  silicate tetrahedra, or the symmetric stretching of the C-O group in  $\text{CaCO}_3$  [27,32]. The shift at  $280\text{ cm}^{-1}$  corresponded to the lattice vibration of the  $\text{CaCO}_3$  [33]. The  $\nu_4$  in-plane bending mode of  $\text{CaCO}_3$  was observed at  $712\text{ cm}^{-1}$  in some pores [34]. The shift at  $1595\text{ cm}^{-1}$  was also attributed to  $\text{CaCO}_3$  [35].



**Figure 3.** Raman spectra of hydration products in different pores (treated by water condition).

By contrast, with 65% RH (Figure 4), the 828 and  $894\text{ cm}^{-1}$  peaks were the characteristic of Raman shifts of  $\text{C}_3\text{S}$  [36,37]. Apart from the signals of unhydrated  $\text{C}_3\text{S}$  and the sheet, the  $1084\text{ cm}^{-1}$  peak was prominent which was consistent with the results of Figure 3. The broad band at  $551\text{ cm}^{-1}$  was due to Si-O-Si stretching modes in  $Q^3$  silicate tetrahedra [32]. The peak at  $519\text{ cm}^{-1}$  resulted from the O-Si-O bending mode in the C-S-H [27,36].



**Figure 4.** Raman spectra of hydration products in different pores (treated by 65% RH condition).

Figure 5 is the Raman spectra of the control. Except for the peaks of unhydrated  $C_3S$  ( $829$  and  $890\text{ cm}^{-1}$ ), the broad shoulder signal near  $513$  and  $558\text{ cm}^{-1}$  were speculated to belong to the antisymmetric bending vibration of O-Si-O in unhydrated  $C_3S$  [37,38]. The peak at  $668\text{ cm}^{-1}$  was characteristic of Si-O-Si symmetrical bending vibration in  $Q^2$  silicate chains of C-S-H. The broad and strong peak at  $1114\text{ cm}^{-1}$  was assigned to the hydroxylated species (Si-OH), which was due to the decrease in the proton numbers which bridged on Si-O of  $Q^2$  silicate tetrahedra [32,38]. The shift at  $355\text{ cm}^{-1}$  was the characteristic band of  $Ca(OH)_2$  [37,38]. The signals around  $1504$  and  $2234\text{ cm}^{-1}$  also belonged to  $Ca(OH)_2$  [39].

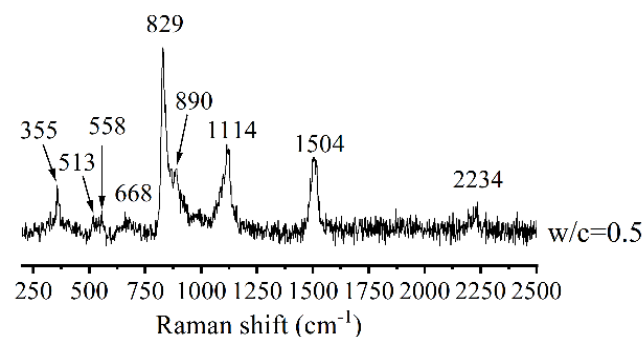


**Figure 5.** Raman spectra of hydration products (the control).

### 3.2. FT-IR

Figure 6 presents the FT-IR spectra of hydration products in the pores of the sheets. There were some characteristic peaks of unhydrated  $C_3S$  in the hydrates of the 65% RH condition and the control. For instance, the  $873\text{ cm}^{-1}$  band with shoulder bands at  $921$  and  $835\text{ cm}^{-1}$  were related to the asymmetric stretching vibrations of Si-O bonds in unhydrated  $C_3S$  [40,41]. Besides some peaks at  $821$ ,  $873$  and  $920\text{ cm}^{-1}$ , the absorption at  $522\text{ cm}^{-1}$  was also attributed to unhydrated  $C_3S$  [40]. In addition, the proximity signal at  $804\text{ cm}^{-1}$  in the curve of water condition was due to Si-O-Si symmetric stretching of  $SiO_2$  [42,43].

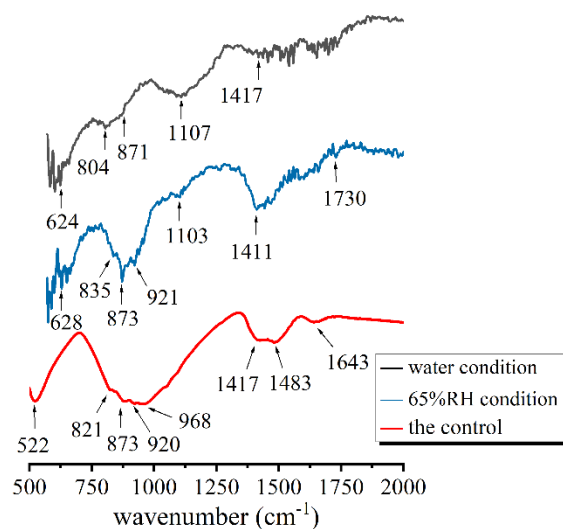


**Figure 6.** FT-IR spectra of hydration products under different hydration conditions.

The hydration results of water condition were similar with those of 65% RH condition. The absorption bands centered at 624 and 628  $\text{cm}^{-1}$  of the two sheets were attributed to Si-O-Si bending vibration in depolymerized structure [44,45]. The broad absorption bands at 1107  $\text{cm}^{-1}$  and 1103  $\text{cm}^{-1}$  were both Si-O stretching vibrations in  $\text{Q}^3$  silicate tetrahedra [40,41,46]. However, the 968  $\text{cm}^{-1}$  band observed in the control was the characteristic of Si-O stretching vibrations in  $\text{Q}^2$  units of C-S-H gel [40,46].

The peaks related to  $\text{Ca}(\text{OH})_2$  and its carbonized products were found in all curves. The absorption at 871  $\text{cm}^{-1}$  was the characteristic vibration mode of carbonate [41,46]. The bands at 1411, 1417 and 1483  $\text{cm}^{-1}$  observed were characteristic of O-C=O symmetric stretching vibrations [47]. The peak at 1730  $\text{cm}^{-1}$  was assigned to the C=O stretching vibrations which were related to the carbonation of  $\text{Ca}(\text{OH})_2$  [45,48]. In addition, The O-H bending vibration signals of water molecules were observed at 1643  $\text{cm}^{-1}$  [46,49].

### 3.3. SEM/EDS

Figure 7 exhibits the SEM images of hydration products under different conditions. It can be seen that the hydration conditions played a prominent role on the morphology of the hydrates. The hydration products in the pore which was treated by the water condition were flake-like, while those treated by the 65% RH condition were honeycomb-like. The morphology of hydration products of the control exhibited interlaced fibers.

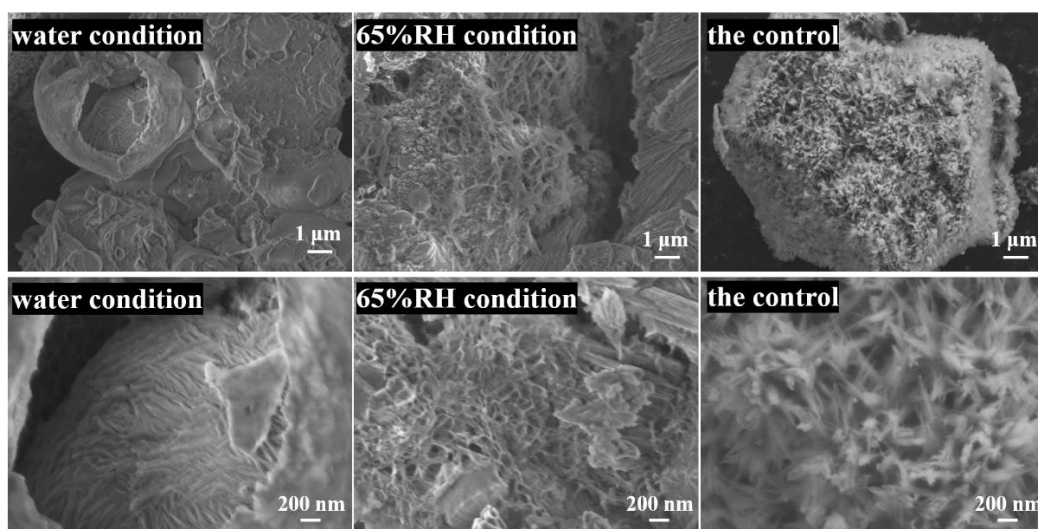


**Figure 7.** SEM images of hydration products under different conditions after 24 h.



The elements in the representative areas in Figure 7 were scanned by EDS and shown in Table 1. Besides the Ti contained in the sheet, the composition of different samples was similar, with calcium and oxygen in the majority. The calcium to silicon ratio (Ca/Si) of the hydration products hydrated by water condition was the highest, followed by that under normal conditions and treated by 65% RH condition.

**Table 1.** EDX analysis of hydration products under different conditions after 24 h (at.%).

Elements	Ca	Si	O	C	Mg	Al	Ti	Ca/Si
water	22.8	8.6	60.9	5.9	0.9	0.3	0.6	2.65
65% RH	33.6	21.2	25.3	8.1	1.1	0.3	9.0	1.58
w/c = 0.5	20.1	10.6	58.8	9.7	0.7	0	0	1.89

#### 4. Discussion

The Raman shifts, FT-IR bands and their distributions observed in the hydration products are summarized in Tables 2 and 3, respectively.

**Table 2.** Raman shifts and distribution of hydration products.

Conditions	Raman Shift (cm <sup>-1</sup> )				
	C <sub>3</sub> S	C-S-H	CaCO <sub>3</sub>	Ca(OH) <sub>2</sub>	Stainless Steel Sheet
water condition (pores)	—	1084 (Q <sup>3</sup> )	280, 713, 1595, 1581 and 1084	—	316, 469, 1449, 1510 and 2425
65% RH condition (pores)	830 and 889	519; 551 and 1084 (Q <sup>3</sup> )	279 and 1084	—	316, 471, 1417, 1511 and 2423
the control (w/c = 0.5)	513, 558, 829 and 890	668 (Q <sup>2</sup> ); and 1114	—	355, 1504 and 2234	—

**Table 3.** FT-IR bands and distribution of hydration products.

Conditions	FT-IR Spectra (cm <sup>-1</sup> )			
	C <sub>3</sub> S	C-S-H	CaCO <sub>3</sub>	Water
water condition (pores)	804	624; 1107 (Q <sup>3</sup> )	871 and 1417	—
65% RH condition (pores)	873, 921 and 835	628; 1103 (Q <sup>3</sup> )	1411 and 1730	—
the control (w/c = 0.5)	522, 821, 873 and 920	968 (Q <sup>2</sup> )	1417 and 1483	1643

Combining the results of Raman and FT-IR spectra, it was clear that the hydration products exhibited a high degree of polymerization dominated by Q<sup>3</sup> silicates for the hydration products in pores. By comparing the hydrates under the water condition and 65% RH condition, the amount of water filling the micropore played no obvious role on the polymeric structure. The difference was that there was still unhydrated C<sub>3</sub>S in the sample which was placed at the 65% RH condition.

SEM and EDS showed the morphology and their Ca/Si ratio of the hydration products in pores. A lower Ca/Si ratio was observed in the sample of the 65% RH condition than in that of the control. This is consistent with previous studies [50,51], which propose that the higher the polymerization degree, the lower the Ca/Si ratio. However, the hydrates under the water condition showed an unexpectedly higher Ca/Si ratio above 2. It lay in the fact that the C-S-H in this region was surrounded by Ca(OH)<sub>2</sub> [52]. It can be confirmed that the oxygen content of products with water condition was higher than those at the 65% RH condition in those testing areas. The flake-like hydration products in this region were

similar to  $\text{Ca}(\text{OH})_2$  [53]. Although the results about the Ca/Si ratio of the products were inconsistent, it is certain that C-S-H gel formed in these micropores. The combinations of the Raman spectra, FT-IR spectra and SEM-EDS results demonstrated that the C-S-H grown in micropores had a high degree of polymerization.

The results of Raman and FT-IR spectra indicated that the C-S-H structure in control obviously grew as  $\text{Q}^2$  silicate tetrahedra. This finding has been confirmed by many scholars [38,40,54,55]. However, the hydration products in the pores showed a higher degree of polymerization ( $\text{Q}^3$ ), and there was almost no characteristic peak of  $\text{Q}^2$  unit. This finding indicates that space restriction affects the structure of the hydration products and the cement which hydrated in the space restriction of micropores tended to form C-S-H with silica tetrahedra of high polymerization degree.

Recently, the space filling hypothesis was opposed by Zajac et al. [56]. They proposed that the slow hydration in the later stage was not due to the effect of restricted space on the further growth of C-S-H, but caused by the slow transport of dissolved ions through the hydrates layer from the dissolution point to the precipitation point [56], and the slow diffusion had an impact on the evolution of the microstructures, such as the fine structure of the inner C-S-H [56]. In this paper, the characterization of the surface hydrates by means of Raman, FT-IR spectra and SEM-EDS indicated that space restriction actually changed the structure of the external hydrates. The influence of space restriction on the growth of C-S-H cannot be ignored, but the relationship between the structure change and the slow diffusion of dissolved ions needs to be further explored. At present, no theory can exclusively dominate the later hydration mechanism. The later stage kinetics is considered to be a combination of multiple mechanisms, such as diffusion mechanism, C-S-H densification and space filling hypothesis [2,13], which requires more research in the future.

## 5. Conclusions

This paper studied the microstructure of  $\text{C}_3\text{S}$  hydrates in the restricted space of micropores in a sheet, by means of Raman, FT-IR spectra and SEM-EDS. Results indicate that space restriction affected the structure of the hydration products, and that the microstructure of the C-S-H which formed in the micropores was mainly composed of  $\text{Q}^3$  silicate tetrahedra with a high degree of polymerization. The amount of water filled in the micropore only affected the hydration degree, rather than the polymeric structure. The C-S-H which formed under conventional conditions mostly existed as a  $\text{Q}^2$  unit. The space restriction of cement hydration is conducive to the formation of C-S-H with silicate tetrahedra of a high polymerization degree.

**Author Contributions:** Conceptualization, Y.Z., Z.W., L.X. and K.W.; methodology, Y.Z., Z.Z. and L.X.; investigation, Y.Z., Z.Z. and Y.C.; writing—original draft preparation, Y.Z.; writing—review and editing, Y.Z., Z.Z., Y.C. and L.X. All authors have read and agreed to the published version of the manuscript.

**Funding:** This research was funded by the fund of National Natural Science Fund of China (No. 51772212), the fund of National Natural Science Fund of China (No. 51978505) and Shanghai Rising Star Program (No. 20QC1400600).

**Institutional Review Board Statement:** Not applicable.

**Informed Consent Statement:** Not applicable.

**Data Availability Statement:** The data presented in this study are available on request from the corresponding author.

**Acknowledgments:** The authors acknowledge greatly the financial support from the fund of National Natural Science Fund of China (51772212), the fund of National Natural Science Fund of China (51978505) and Shanghai Rising Star Program (20QC1400600). Additionally, thanks are extended to the anonymous reviewers whose suggestions improved this manuscript.

**Conflicts of Interest:** The authors declare no conflict of interest.



## References

1. Allen, A.J.; Thomas, J.J.; Jennings, H.M. Composition and density of nanoscale calcium-silicate-hydrate in cement. *Nat. Mater.* **2007**, *6*, 311–316. [[CrossRef](#)] [[PubMed](#)]
2. Scrivener, K.; Ouzia, A.; Juilland, P.; Mohamed, A.K. Advances in understanding cement hydration mechanisms. *Cem. Concr. Res.* **2019**, *124*, 105823. [[CrossRef](#)]
3. Sato, M.; Umemura, Y.; Koizumi, K. Effect of water-binder ratio on silicate structure and hydration of silicafume cement. *Cem. Sci. Concr. Technol.* **2011**, *65*, 456–463. [[CrossRef](#)]
4. Tanaka, Y.; Saeki, T.; Sasaki, K.; Suda, Y. Fundamental study on density of C-S-H. *Cem. Sci. Concr. Technol.* **2009**, *63*, 70–76. [[CrossRef](#)]
5. Gallucci, E.; Zhang, X.; Scrivener, K.L. Effect of temperature on the microstructure of calcium silicate hydrate (C-S-H). *Cem. Concr. Res.* **2013**, *53*, 185–195. [[CrossRef](#)]
6. Okada, Y.; Ishida, H.; Sasaki, K.; Young, J.; Mitsuda, T. Characterization of C-S-H from highly reactive  $\beta$ -dicalcium silicate prepared from hillebrandite. *J. Am. Ceram. Soc.* **1994**, *77*, 1313–1318. [[CrossRef](#)]
7. Martínez-Ramírez, S.; Frías, M. The effect of curing temperature on white cement hydration. *Constr. Build. Mater.* **2009**, *23*, 1344–1348. [[CrossRef](#)]
8. Xu, L.; Tang, C.; Li, H.; Wu, K.; Zhang, Y.; Yang, Z. Hydration characteristics assessment of a binary calcium sulfoaluminate-anhydrite cement related with environment temperature. *J. Therm. Anal. Calorim.* **2021**. [[CrossRef](#)]
9. Narattha, C.; Chaipanich, A. Effect of curing time on the hydration and material properties of cold-bonded high-calcium fly ash–Portland cement lightweight aggregate. *J. Therm. Anal. Calorim.* **2020**. [[CrossRef](#)]
10. Wu, K.; Han, H.; Xu, L.; Gao, Y.; Yang, Z.; Jiang, Z.; De Schutter, G. The improvement of freezing–thawing resistance of concrete by cellulose/polyvinyl alcohol hydrogel. *Constr. Build. Mater.* **2021**, *291*, 123274. [[CrossRef](#)]
11. Schönlein, M.; Plank, J. A TEM study on the very early crystallization of C-S-H in the presence of polycarboxylate superplasticizers: Transformation from initial C-S-H globules to nanofoils. *Cem. Concr. Res.* **2018**, *106*, 33–39. [[CrossRef](#)]
12. Bazzoni, A. Study of Early Hydration Mechanisms of Cement by Means of Electron Microscopy. Ph.D. Thesis, École Polytechnique Fédérale de Lausanne, Lausanne, Switzerland, 2014.
13. Ouzia, A.R.C.W.C. Modeling the Kinetics of the Main Peak and Later Age of Alite Hydration. Ph.D. Thesis, École Polytechnique Fédérale de Lausanne, Lausanne, Switzerland, 2019.
14. Bullard, J.W.; Jennings, H.M.; Livingston, R.A.; Nonat, A.; Scherer, G.W.; Schweitzer, J.S.; Scrivener, K.L.; Thomas, J.J. Mechanisms of cement hydration. *Cem. Concr. Res.* **2011**, *41*, 1208–1223. [[CrossRef](#)]
15. Berodier, E.; Scrivener, K. Evolution of pore structure in blended systems. *Cem. Concr. Res.* **2015**, *73*, 25–35. [[CrossRef](#)]
16. Xu, L.; Ou, Y.; Hecker, A.; Rößler, C.; Ludwig, H.M.; Yang, Z.; Wu, K. State of water in calcium sulfoaluminate cement paste modified by hydroxyethyl methyl cellulose ether. *J. Build. Eng.* **2021**, 102894. [[CrossRef](#)]
17. Scherer, G.W. Stress from crystallization of salt. *Cem. Concr. Res.* **2004**, *34*, 1613–1624. [[CrossRef](#)]
18. Wenzel, O.; Schwotzer, M.; Müller, E.; Chakravadhanula, V.S.K.; Scherer, T.; Gerdes, A. Investigating the pore structure of the calcium silicate hydrate phase. *Mater. Charact.* **2017**, *133*, 133–137. [[CrossRef](#)]
19. Li, H.; Xue, Z.; Liang, G.; Wu, K.; Dong, B.; Wang, W. Effect of C-S-Hs-PCE and sodium sulfate on the hydration kinetics and mechanical properties of cement paste. *Constr. Build. Mater.* **2021**, *266*, 121096. [[CrossRef](#)]
20. Jennings, H.M. A model for the microstructure of calcium silicate hydrate in cement paste. *Cem. Concr. Res.* **2000**, *30*, 101–116. [[CrossRef](#)]
21. Jennings, H.M. Refinements to colloid model of C-S-H in cement: CM-II. *Cem. Concr. Res.* **2008**, *38*, 275–289. [[CrossRef](#)]
22. Similauer, V.; Bittnar, Z.K. Microstructure-based micromechanical prediction of elastic properties in hydrating cement paste. *Cem. Concr. Res.* **2006**, *36*, 1708–1718. [[CrossRef](#)]
23. Königsberger, M.; Hellmich, C.; Pichler, B. Densification of C-S-H is mainly driven by available precipitation space, as quantified through an analytical cement hydration model based on NMR data. *Cem. Concr. Res.* **2016**, *88*, 170–183. [[CrossRef](#)]
24. Constantinides, G.; Ulm, F.-J. The effect of two types of C-S-H on the elasticity of cement-based materials: Results from nanoindentation and micromechanical modeling. *Cem. Concr. Res.* **2004**, *34*, 67–80. [[CrossRef](#)]
25. Farhadi, N.; Peyvandi, A.; Holmes, D.; Soroushian, P.; Balachandra, A.M. Effects of Graphite Nanoplatelets on the Structure of Cementitious Materials. *Iran. J. Sci. Technol. Trans. Civ. Eng.* **2019**, *43*, 403–411. [[CrossRef](#)]
26. Richardson, I.G. The nature of the hydration products in hardened cement pastes. *Cem. Concr. Compos.* **2000**, *22*, 97–113. [[CrossRef](#)]
27. Kirkpatrick, R.J.; Yarger, J.L.; McMillan, P.F.; Ping, Y.; Cong, X. Raman spectroscopy of C-S-H, tobermorite, and jennite. *Adv. Cem. Based Mater.* **1997**, *5*, 93–99. [[CrossRef](#)]
28. Cong, X.; Kirkpatrick, R.J. <sup>29</sup>Si MAS NMR study of the structure of calcium silicate hydrate. *Adv. Cem. Based Mater.* **1996**, *3*, 144–156. [[CrossRef](#)]
29. Rodriguez, E.T.; Richardson, I.G.; Black, L.; Boehm-Courjault, E.; Nonat, A.; Skibsted, J. Composition, silicate anion structure and morphology of calcium silicate hydrates (C-S-H) synthesised by silica-lime reaction and by controlled hydration of tricalcium silicate (C3S). *Adv. Appl. Ceram.* **2015**, *114*, 362–371. [[CrossRef](#)]
30. Thomas, J.J.; Jennings, H.M. A colloidal interpretation of chemical aging of the C-S-H gel and its effects on the properties of cement paste. *Cem. Concr. Res.* **2006**, *36*, 30–38. [[CrossRef](#)]

31. Jennings, H.M. Colloid model of C–S–H and implications to the problem of creep and shrinkage. *Mater. Struct.* **2004**, *37*, 59–70. [[CrossRef](#)]
32. Ortaboy, S.; Li, J.; Geng, G.; Myers, R.J.; Monteiro, P.J.M.; Maboudian, R.; Carraro, C. Effects of CO<sub>2</sub> and temperature on the structure and chemistry of C–(A)–S–H investigated by Raman spectroscopy. *RSC Adv.* **2017**, *7*, 48925–48933. [[CrossRef](#)]
33. Potgieter-Vermaak, S.S.; Potgieter, J.H.; Belleil, M.; Deweerdt, F.; Grieken, R.V. The application of Raman spectrometry to the investigation of cement: Part II: A micro-Raman study of OPC, slag and fly ash. *Cem. Concr. Res.* **2006**, *36*, 663–670. [[CrossRef](#)]
34. Bai, Y.; Guo, X.-j.; Li, Y.-z.; Huang, T. Experimental and visual research on the microbial induced carbonate precipitation by *Pseudomonas aeruginosa*. *Amb Express* **2017**, *7*, 57. [[CrossRef](#)]
35. Podborodnikov, I.; Shatskiy, A.; Arefiev, A.; Rashchenko, S.; Chanyshv, A.; Litasov, K. The system Na<sub>2</sub>CO<sub>3</sub>–CaCO<sub>3</sub> at 3 GPa. *Phys. Chem. Miner.* **2018**, *45*, 773–787. [[CrossRef](#)]
36. Liu, F.; Sun, Z.; Qi, C. Raman spectroscopy study on the hydration behaviors of Portland cement pastes during setting. *J. Mater. Civ. Eng.* **2014**, *27*, 04014233. [[CrossRef](#)]
37. Tarrida, M.; Madon, M.; Le Rolland, B.; Colombet, P. An in-situ Raman spectroscopy study of the hydration of tricalcium silicate. *Adv. Cem. Based Mater.* **1995**, *2*, 15–20. [[CrossRef](#)]
38. Garbev, K.; Stemmermann, P.; Black, L.; Breen, C.; Yarwood, J.; Gasharova, B. Structural features of C-S-H(I) and its carbonation in air—A Raman spectroscopic study. Part I: Fresh phases. *J. Am. Ceram. Soc.* **2007**, *90*, 900–907. [[CrossRef](#)]
39. Liu, F.J.; Sun, Z.H. Chemical mapping of cement pastes by using confocal Raman spectroscopy. *Front. Struct. Civ. Eng.* **2016**, *10*, 168–173. [[CrossRef](#)]
40. del Bosque, I.F.S.; Martinez-Ramirez, S.; Blanco-Varela, M.T. FTIR study of the effect of temperature and nanosilica on the nanostructure of C-S-H gel formed by hydrating tricalcium silicate. *Constr. Build. Mater.* **2014**, *52*, 314–323. [[CrossRef](#)]
41. Choudhary, H.K.; Anupama, A.V.; Kumar, R.; Panzi, M.E.; Matteppanavar, S.; Sherikar, B.N.; Sahoo, B. Observation of phase transformations in cement during hydration. *Constr. Build. Mater.* **2015**, *101*, 122–129. [[CrossRef](#)]
42. Al-Maliki, F. Detection of Random Laser Action from Silica Xerogel Matrices Containing Rhodamine 610 Dye and Titanium Dioxide Nanoparticles. *Adv. Mater. Phys. Chem.* **2012**, *2*, 110–115. [[CrossRef](#)]
43. Ramalla, I.; Gupta, R.; Bansal, K. Effect on superhydrophobic surfaces on electrical porcelain insulator, improved technique at polluted areas for longer life and reliability. *Int. J. Eng. Technol.* **2015**, *4*, 509–519. [[CrossRef](#)]
44. Darmakkolla, S.R.; Tran, H.; Gupta, A.; Ranavavare, S.B. A method to derivatize surface silanol groups to Si-alkyl groups in carbon-doped silicon oxides. *RSC Adv.* **2016**, *6*, 93219–93230. [[CrossRef](#)]
45. Grill, A.; Neumayer, D.A. Structure of low dielectric constant to extreme low dielectric constant SiCOH films: Fourier transform infrared spectroscopy characterization. *J. Appl. Phys.* **2003**, *94*, 6697–6707. [[CrossRef](#)]
46. Fernandez, L.; Alonso, C.; Hidalgo, A.; Andrade, C. The role of magnesium during the hydration of C<sub>3</sub>S and C-S-H formation. Scanning electron microscopy and mid-infrared studies. *Adv. Cem. Res.* **2005**, *17*, 9–21. [[CrossRef](#)]
47. Bonnier, F.; Blasco, H.; Wasselet, C.; Brachet, G.; Respaud, R.; Carvalho, L.F.C.S.; Bertrand, D.; Baker, M.J.; Byrne, H.J.; Chourpa, I. Ultra-filtration of human serum for improved quantitative analysis of low molecular weight biomarkers using ATR-IR spectroscopy. *Analyst* **2017**, *142*, 1285–1298. [[CrossRef](#)]
48. Das, I.; Mishra, M.K.; Medda, S.K.; De, G. Durable superhydrophobic ZnO-SiO<sub>2</sub> films: A new approach to enhance the abrasion resistant property of trimethylsilyl functionalized SiO<sub>2</sub> nanoparticles on glass. *RSC Adv.* **2014**, *4*, 54989–54997. [[CrossRef](#)]
49. Kalkan, E.; Nadaroglu, H.; Celebi, N.; Tozsın, G. Removal of textile dye Reactive Black 5 from aqueous solution by adsorption on laccase-modified silica fume. *Desalin. Water Treat.* **2014**, *52*, 6122–6134. [[CrossRef](#)]
50. He, Y.; Zhao, X.; Lu, L.; Struble, L.J.; Hu, S. Effect of C/S ratio on morphology and structure of hydrothermally synthesized calcium silicate hydrate. *J. Wuhan Univ. Technol. Mater. Sci. Ed.* **2011**, *26*, 770–773. [[CrossRef](#)]
51. He, Y.; Lu, L.; Struble, L.J.; Rapp, J.L.; Mondal, P.; Hu, S. Effect of calcium–silicon ratio on microstructure and nanostructure of calcium silicate hydrate synthesized by reaction of fumed silica and calcium oxide at room temperature. *Mater. Struct.* **2014**, *47*, 311–322. [[CrossRef](#)]
52. Hu, Q.N.; Aboustait, M.; Kim, T.; Ley, M.T.; Hanan, J.C.; Bullard, J.; Winarski, R.; Rose, V. Direct three-dimensional observation of the microstructure and chemistry of C<sub>3</sub>S hydration. *Cem. Concr. Res.* **2016**, *88*, 157–169. [[CrossRef](#)]
53. García Carmona, J.; Gómez Morales, J.; Rodríguez Clemente, R. Rhombohedral–scalenoedra calcite transition produced by adjusting the solution electrical conductivity in the system Ca(OH)<sub>2</sub>–CO<sub>2</sub>–H<sub>2</sub>O. *J. Colloid Interface Sci.* **2003**, *261*, 434–440. [[CrossRef](#)]
54. Masmoudi, R.; Kupwade-Patil, K.; Bumajdad, A.; Buyukozturk, O. In situ Raman studies on cement paste prepared with natural pozzolanic volcanic ash and Ordinary Portland Cement. *Constr. Build. Mater.* **2017**, *148*, 444–454. [[CrossRef](#)]
55. Dariz, P.; Schmid, T. Ferruginous phases in 19th century lime and cement mortars: A Raman microspectroscopic study. *Mater. Charact.* **2017**, *129*, 9–17. [[CrossRef](#)]
56. Zajac, M.; Skocek, J.; Lothenbach, B.; Mohsen, B.H. Late hydration kinetics: Indications from thermodynamic analysis of pore solution data. *Cem. Concr. Res.* **2020**, *129*, 105975. [[CrossRef](#)]